

Single-Atom Cu Catalysts for Enhanced Electrocatalytic Nitrate Reduction with Significant Alleviation of Nitrite Production

Tonghe Zhu, Qiongsan Chen, Peng Liao, Weijian Duan, Sheng Liang, Zhang Yan, and Chunhua Feng*

Metallic Cu is a well-known electrocatalyst for nitrate reduction reaction (NO₃RR), but it suffers from relatively low activity, poor stability, and inducing nitrite accumulation during the long-term operation. Herein, it is found that Cu catalysts minimized at the single-atom level can overcome the limitations of bulk materials in NO₃RR. A metal-nitrogen-carbon (M-N-C) electrocatalyst composed of carbon nanosheets embedding isolated copper atoms coordinated with N, Cu-N-C-800, is synthesized by pyrolysis of a Cu-based metal-organic framework at 800 °C. In comparison with Cu nanoparticles and Cu plate-800, kinetic measurements show that the Cu-N-C-800 electrocatalyst is more active and stable and distinctly suppresses the release of nitrite intermediate into the solution. The combined results of experimental data and density functional theory calculations indicate that Cu bound with N (particularly Cu-N₂) is the key to favorable adsorption of NO₃⁻ and NO₂⁻. This strong binding is responsible for the enhanced rate of nitrate conversion to the end products of ammonia and nitrogen. These findings highlight the promise of single-atom Cu electrocatalysts for nitrate reduction with desirable performance.

1. Introduction

Nitrate pollution in surface water and groundwater is widespread in the world, including in the United States, China, and Europe, originating from fertilizer runoff, stormwater runoff, and improper discharge of wastewater from industries (e.g., fertilizer, nuclear, and metal finishing factories).^[1] High concentrations of nitrate in aquatic ecosystems pose


a serious threat to ecological balances and human health. To minimize such adverse effects, many approaches have been utilized to eliminate nitrate from water. Biological denitrification^[2] is the most widely used process due to its cost-effectiveness, but it suffers the technical problems of excessive sludge production, low reaction rates, and high demand for a carbon source. Physical approaches, such as reverse osmosis,^[3] ion exchange,^[4] electro dialysis,^[5] and membrane filtration,^[6] are effective in separating nitrate at high rates but are expensive and lead to the creation of secondary nitrate-laden wastewater that needs to be treated. Ideally, electrocatalytic denitrification driven by “green” electricity from renewable resources is a promising alternative that can overcome those limitations; as such, it is an area of intense study.^[7–10] Nitrate with an oxidation valence of +5 can be electrocatalytically reduced to a variety of

nitrogen products with oxidation valences from +3 to -3, such as nitrite, nitric oxide, nitrous oxide, nitrogen, hydroxylamine, and ammonia.^[11,12] An electrocatalyst plays an essential role in nitrate reduction reaction (NO₃RR) and significantly influences the form of the product. From the perspective of environmental scientists, the most desirable solution for nitrate removal is to selectively reduce it to harmless gaseous nitrogen, but few non-noble metal catalysts available today can convert nitrate into nitrogen with a high selectivity. In this regard, recent studies^[13–16] by chemical scientists have attempted to promote the selectively electrocatalytic reduction of nitrate to ammonia, a value-added product utilized as a precursor to fertilizer.

Cu-based electrocatalysts have been widely investigated in NO₃RR to produce nitrogen and ammonia due to their superior electrochemical activity, tunable electronic structure, and low cost.^[11,15,17] However, two issues must be addressed in connection with Cu electrocatalysts. One is associated with catalyst deactivation after long-term operation due to passivation, leaching, and corrosion; the other is the accumulation of nitrite,^[12,17–19] a main quasi-stable intermediate that is a carcinogen and more toxic than nitrate during the process of NO₃RR. Prolonged electrolysis and enhanced current density can further reduce nitrite and promote its conversion to nitrogen and ammonia, but these procedures result in higher

T. Zhu, Q. Chen, W. Duan, S. Liang, Z. Yan, Prof. C. Feng
The Key Lab of Pollution Control and Ecosystem Restoration
in Industry Clusters
Ministry of Education
School of Environment and Energy
South China University of Technology
Guangzhou 510006, P. R. China
E-mail: chfeng@scut.edu.cn

Prof. P. Liao
The State Key Laboratory of Environmental Geochemistry
Institute of Geochemistry
Chinese Academy of Sciences
Guiyang 550081, P. R. China

 The ORCID identification number(s) for the author(s) of this article can be found under <https://doi.org/10.1002/smll.202004526>.

DOI: 10.1002/smll.202004526

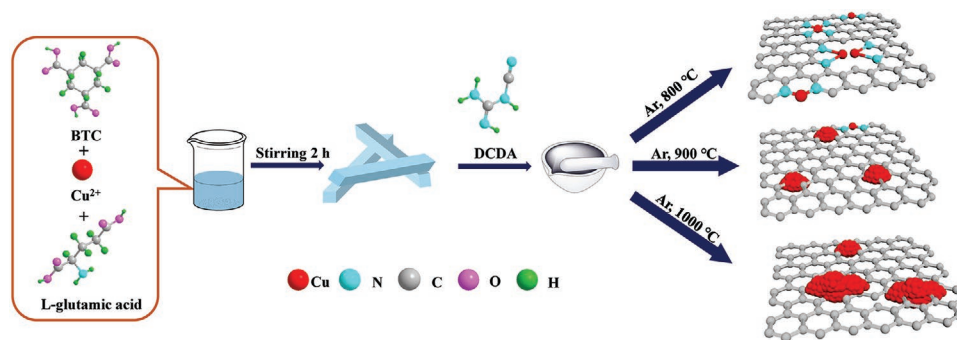
energy consumption. The above issues highlight the need to develop highly effective, selective, and stable electrocatalysts to drive NO₃RR with a low applied current, a short electrolysis time, and desirable products. Downsizing the metal particles into single atoms should be a promising strategy to meet this need because single-atom catalysis, as a new frontier in electrocatalysis, has recently attracted increasing attention due to its maximum atom-utilization efficiency and superior catalytic performance.^[20] It offers desirable advantages, including: i) increased activity owing to fully exposed active atoms and low-coordination metal centers that facilitate adsorption and conversion of reactive species;^[21] ii) enhanced selectivity attributed to the homogeneous active sites and geometric structure, which allows uniform interaction with substrates;^[21,22] and iii) appreciable stability because of the strong interactions between single atoms and surrounding coordination atoms that protect and stabilize single atomic metals.^[23,24]

In this study, we made a first attempt to show that a catalyst composed of single Cu atoms anchored on nitrogenated carbon nanosheets (Cu-N-C) exhibits outstanding activity and stability in NO₃RR. More importantly, we found that this catalyst enables significant alleviation of nitrite production, which is often observed for metallic Cu catalysts, either in the form of nanoparticles or films.^[19,25–27] To evaluate the electrocatalytic performance of Cu-N-C in terms of mass activity, selectivity, and long-term durability, and to theoretically identify the active sites responsible for this, a combination of surface characterizations, batch electrolysis tests, and density functional theory (DFT) calculations were conducted.

2. Results and Discussion

2.1. Structural Characterizations of Catalysts

The Cu-N-C catalysts were synthesized via pyrolysis in an Ar environment, starting from a mixture precursor containing a Cu-MOF (Scheme 1). The Cu-MOF (Figure S1, Supporting Information) was obtained from liquid-phase reaction between Cu(CO₂CH₃)₂H₂O, L-glutamic acid, trimesic acid, and dicyandiamide that were important for stabilizing metal atoms and creating the sheet structure. The as-obtained samples were labeled as Cu-N-C-*T*, where *T* is the annealing temperature, an important factor to tailor the size of Cu in the nanosheet.



Scheme 1. Schematic illustration of the synthesis process for Cu-N-C-*T*.

Figure 1 and Figures S2–S4 (Supporting Information) present and compare the morphology and composition of the obtained Cu-N-C samples. The Cu-N-C-800 exhibited a 2D carbon nanosheet structure with wrinkles (Figure 1a). The high-angle annular dark field (HAADF)-scanning transmission electron microscope (STEM) and the relevant elemental mapping images revealed the existence and highly uniform distribution of C, N, and Cu atoms in Cu-N-C-800 (Figure 1b). Additional double aberration-corrected (AC) HAADF-STEM images are provided in Figure 1c,d. Bright dots attributed to Cu atoms were clearly observable on the carbon nanosheets of Cu-N-C-800, confirming the successful synthesis of single Cu atoms anchored on the carbon matrix as previously shown.^[28] As illustrated in Figure S2a–c (Supporting Information), the Cu-N-C-700 exhibited a similar nanosheet structure and the C, N, and Cu atoms were also detected in it. However, there were no visible bright dots in the (AC) HAADF-STEM image, possibly because the single Cu atoms were covered by the thick carbon nanosheets. The increasing pyrolysis temperature (i.e., 900 and 1000 °C) led to the aggregation of some Cu atoms, partly appearing in the form of nanoparticles or clusters (Figure 1e–h and Figure S2d–f, Supporting Information). Compared with Cu-N-C-1000, the Cu-N-C-900 sample presented smaller nanoparticles with a mean size of 50 nm. It should be noted that the weight ratios of Cu in the samples did not vary significantly and were 24.49%, 25.12%, 23.24%, and 21.58% in relation to Cu-N-C-700/800/900/1000, respectively. The high content of Cu (more than 20%) in all the Cu-N-C-*T* samples is attributed to the use of dicyandiamide, which provides high-density N-coordination sites to firmly trap Cu during the pyrolysis, analogous to the previous reports on obtaining high loadings of atomic metals by stabilizing them with N or P moieties.^[29,30]

The crystalline structure and chemical state of Cu-N-C-800 and the reference samples were further identified by X-ray diffractometry (XRD) patterns and X-ray photoelectron spectrometer (XPS) measurements. Figure 1i and Figure S3a (Supporting Information) show that the Cu-N-C-700, Cu-N-C-800, and N-C-800 samples exhibited only one broad peak at 26° assigned to the (002) plane of graphitic carbon. No characteristic peaks for metallic Cu or its oxides were discerned in Cu-N-C-700/800, further supporting the presence of highly dispersed Cu-containing species on the carbon nanosheets without aggregation. Conversely, for the Cu-N-C-900 and Cu-N-C-1000

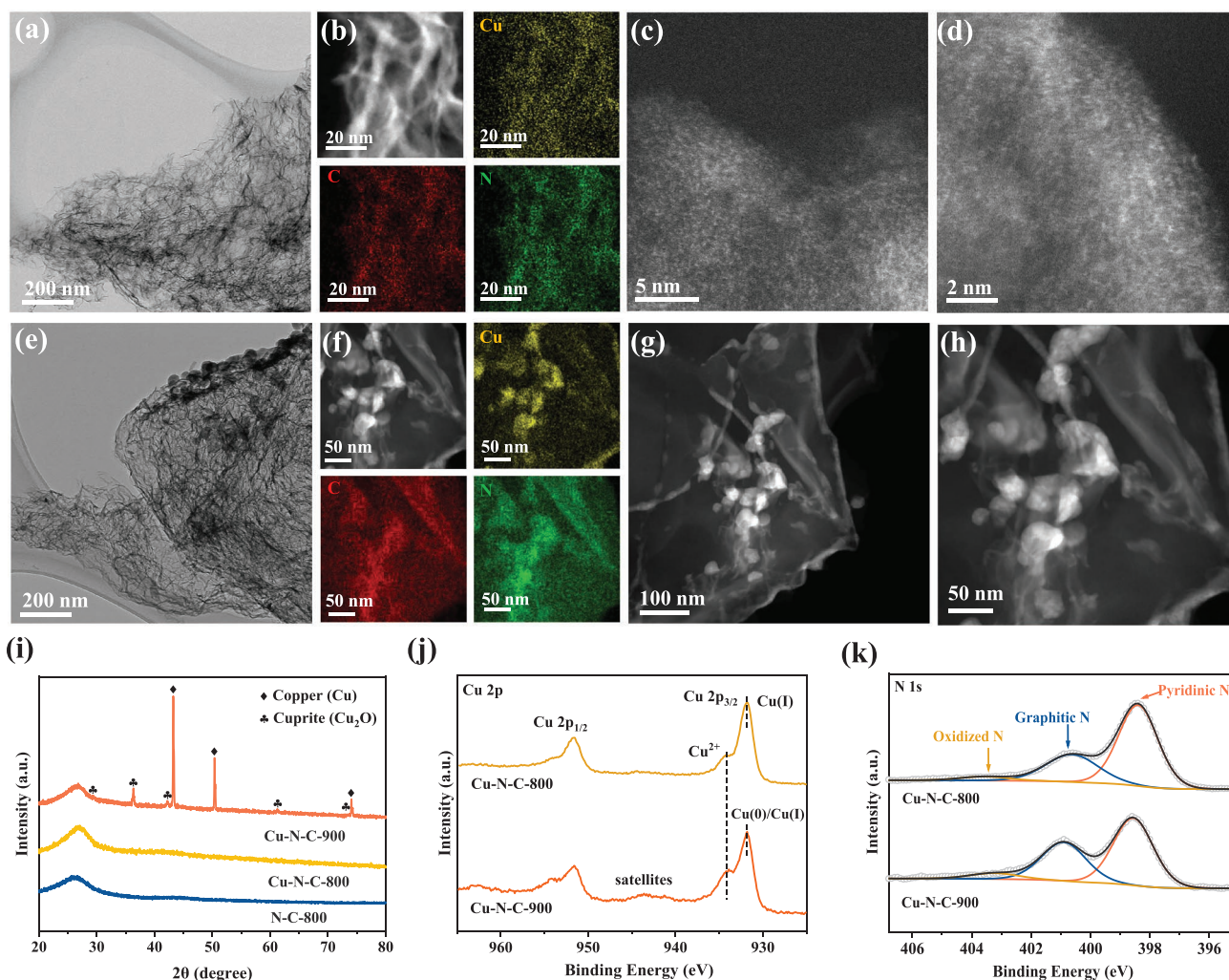


Figure 1. The morphology and structural characterizations of a–d) Cu-N-C-800 and e–h) Cu-N-C-900: a,e) TEM images; b,f) HAADF-STEM and energy-dispersive X-ray spectroscopy (EDX) mapping images; c,d) aberration-corrected (AC) HAADF-STEM images; and g,h) HAADF-STEM images. i) XRD patterns, j) Cu 2p and k) N 1s XPS spectra of different samples.

samples (Figure 1i and Figure S3b, Supporting Information), three sharp diffraction peaks were observed at $\approx 43.4^\circ$, $\approx 50.3^\circ$, and $\approx 73.9^\circ$, assigned to the (111), (200), and (220) planes of the face-centered cubic phase of Cu, respectively. This indicates the presence of zero-valence Cu particles, in good agreement with the related HAADF-STEM results. As shown in the XPS data (Figure 1j and Figure S4a,b, Supporting Information), the Cu 2p_{3/2} spectrum was deconvoluted into two peaks at binding energies of 932.3 and 934.5 eV, suggesting that there are two chemical states in Cu-N-C-700/800/900/1000. The peak located at 934.5 eV is assigned to the Cu(II) species,^[31] and the peak at 932.3 eV probably corresponds to the Cu(0) and/or Cu(I) species.^[32] The N 1s XPS peak (Figure 1k) could be fitted with three contributions located at 398.3, 400.6, and 403.5 eV, assigned to pyridinic N, graphitic N, and oxidized N species, respectively. Notably, the Cu-N-C-700/800 samples exhibited higher atomic ratio of pyridinic N (Table S1, Supporting Information). It has been reported that the pyridinic N sites are conducive to coordination with single-atom metals.^[33,34]

Further studies of X-ray absorption near edge structure (XANES) and extended X-ray absorption fine structure (EXAFS) were performed to obtain information on the electronic structure and coordination environment of Cu species in Cu-N-C-800 and Cu-N-C-900. The standard Cu foil and copper(II) phthalocyanine (CuPc) samples were utilized as the reference. As illustrated in Figure 2a, the Cu-K absorption edge and transition energies of Cu-N-C-800/900 were higher than that of Cu foil and lower than that of CuPc, an indication of the Cu valence between Cu(0) and Cu(II). Figure 2b shows and compares the Fourier transform (FT) EXAFS analysis curves of different samples. The Cu-N-C-800 displayed a main peak at ≈ 1.5 Å, a location analogous to that observed in CuPc and attributed to the Cu–N bond.^[31] The peak at ≈ 2.2 Å assigned to the Cu–Cu bond (which distinctly appeared in Cu foil) was not observable. This phenomenon suggests that the Cu atoms are predominantly bonded with N atoms in Cu-N-C-800, a finding consistent with the HAADF-STEM and XRD results. For Cu-N-C-900, both the Cu–N bond and the Cu–Cu

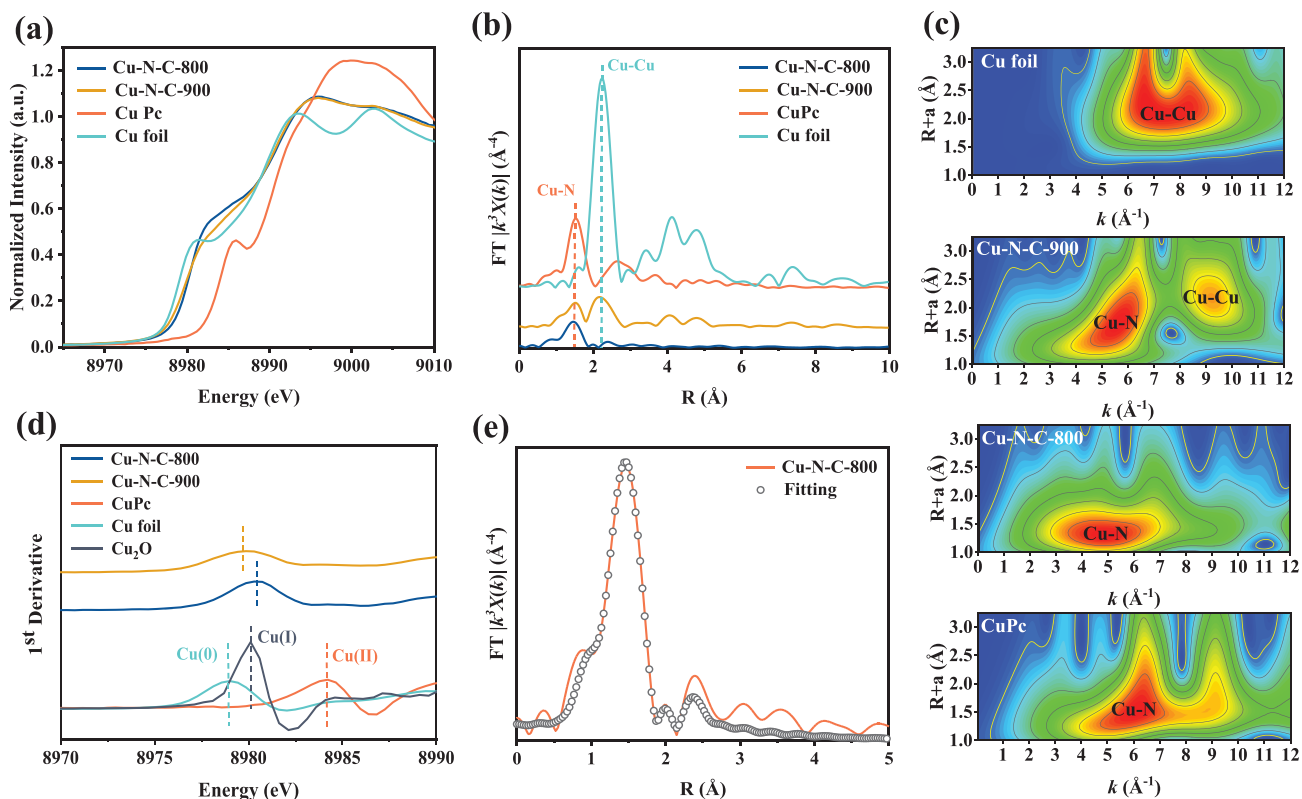


Figure 2. a) Cu K-edge XANES spectra; b) FT-EXAFS spectra; c) WT-EXAFS spectra; and d) first derivative of XANES of Cu-N-C-800, Cu-N-C-900, and references. e) Corresponding FT-EXAFS fitting curves of Cu-N-C-800.

bond existed, possibly due to the breaking of the Cu–N bond and the partial formation of Cu nanoparticles as a consequence of the increasing annealing temperature. The wavelet transform (WT) plots (Figure 2c) further identify the different coordination state of Cu sites and corroborate the existence of the sole Cu–N bond in Cu-N-C-800 and the change of a certain amount of the Cu–N bond to a Cu–Cu bond in Cu-N-C-900. In Figure 2d, the first derivative of the XANES curves of Cu-N-C-800/900 was presented and compared with the standard Cu foil, CuPc, and Cu₂O samples. The distinct peak of Cu-N-C-800 was located between the characteristic peaks of CuPc and Cu₂O, whereas the peak of Cu-N-C-900 was located between those of Cu₂O and Cu foil. This suggests that the Cu species in Cu-N-C-800 has a mixed valence between Cu(I) and Cu(II) and that in Cu-N-C-900 exhibits a mixed valence between Cu(0) and Cu(I). Notably, the peak positions of Cu-N-C-800/900 were relatively close to the Cu(I) peak of Cu₂O, indicating the predominance of Cu(I) that is likely coordinated with N atoms in the Cu–N structures. Figure 2e illustrates the FT-EXAFS spectrum of the Cu-N-C-800, which could be fitted with the proposed Cu–N₂ and Cu–N₄ mixed structures on the basis of the fitting parameters listed in Table S2 (Supporting Information). This is in accordance with the XPS result proving the existence of Cu(I) and Cu(II), because the valence states of Cu in Cu–N₂ and Cu–N₄ moieties are Cu(I) and Cu(II), respectively.^[35,36]

2.2. Electrocatalytic Denitrification Performance of Catalysts

To evaluate the capacity of Cu-N-C for electrocatalytic NO₃RR and determine the size effect of Cu, the electrochemical performance of the nickel foam (NF) electrodes equipped with the Cu-N-C-700, Cu-N-C-800, Cu-N-C-900, Cu-N-C-1000, and N-C-800 samples and the Cu plate-800 electrode was examined and compared. The reference Cu plate-800, as bulk metallic Cu with high purity, represents the typical copper electrode for NO₃RR, possibly having inevitable shortcomings of passivation, corrosion, and undesirable by-products. Figure 3a shows the time courses of NO₃[−]-N proportion as a consequence of different cathodes. Insignificant proportions of NO₃[−]-N disappeared in the cases of bare NF (from initial 50.0 to 48.9 mg L^{−1}) and N-C-800-coated NF (from initial 50.0 to 49.3 mg L^{−1}) after 12 h of operation, indicating the inactivity of NF and N-C-800 in catalyzing nitrate reduction and the insignificant adsorption of NO₃[−] onto them. The Cu plate-800 cathode was active in facilitating nitrate reduction, which allowed the transformation of 24.6% of the NO₃[−]-N at 12 h. The Cu-N-C-*T* cathodes enabled appreciably higher amounts of NO₃[−]-N conversion within 12 h, with the Cu-N-C-800 exhibiting superior electrocatalytic performance (a conversion yield of 97.3%). All of the reactions obeyed the pseudo-first-order kinetics, and the apparent rate constants were calculated according to the integrated rate law by fitting the NO₃[−]-N concentration versus time profiles. The

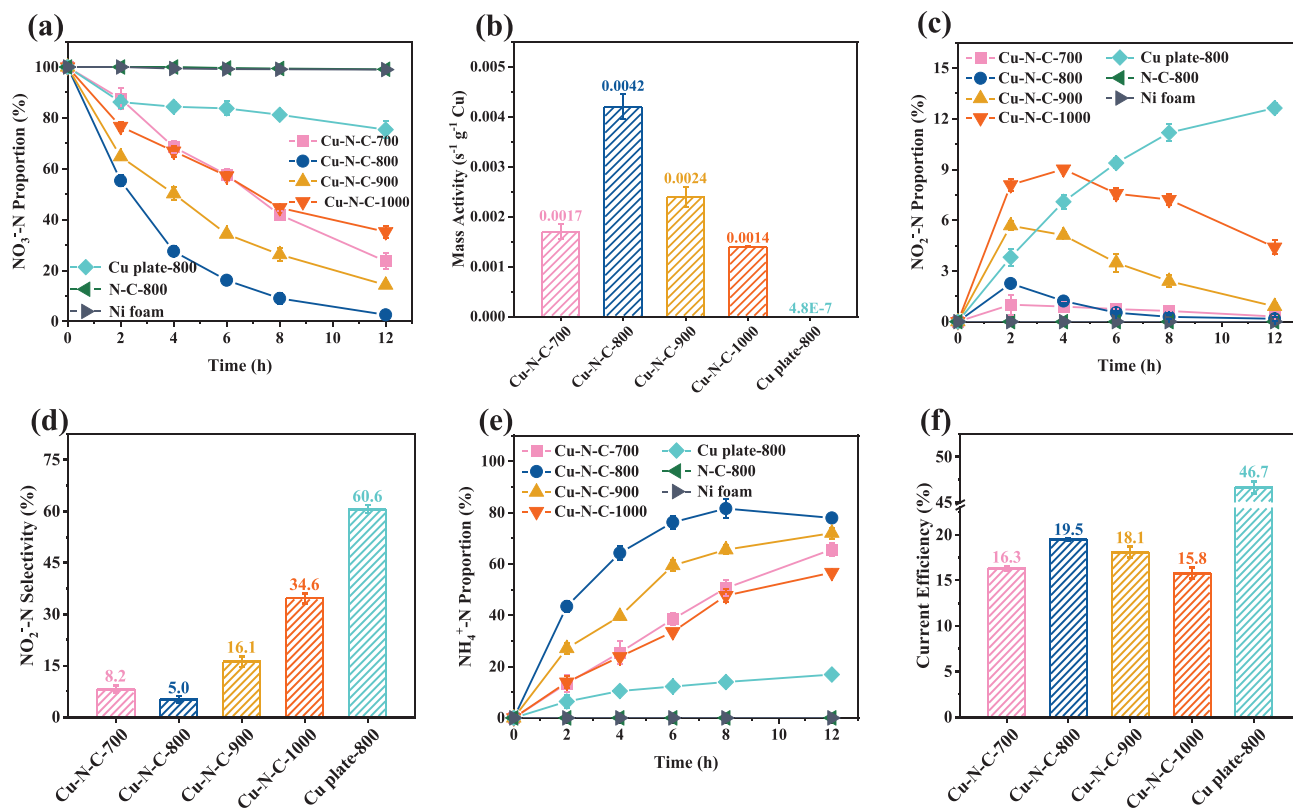


Figure 3. Comparisons of a) time-course NO₃⁻-N proportion; b) mass activity; c) time-course NO₂⁻-N proportion; d) NO₂⁻-N selectivity; e) time-course NH₄⁺-N proportion; and f) current efficiency between different cathodes in NO₃RR. For (d), the highest NO₂⁻-N selectivity was recorded throughout the electrolysis process. Reaction conditions: [initial NO₃⁻-N] = 50 mg L⁻¹; [Na₂SO₄] = 50 × 10⁻³ M; cathodic potential = -1.3 V; and electrolysis time = 12 h.

values associated with the Cu-N-C-700, Cu-N-C-800, Cu-N-C-900, Cu-N-C-1000, and Cu plate-800 cathodes were 3.38×10^{-5} , 8.40×10^{-5} , 4.42×10^{-5} , 2.40×10^{-5} , and 5.27×10^{-6} s⁻¹, respectively (Figure S5, Supporting Information). The mass activity of the catalysts was determined by normalizing the rate constant to the weight of Cu contained in the cathode. As depicted in Figure 3b, the Cu-N-C-800 cathode achieved a mass activity of 4.2×10^{-3} s⁻¹ g⁻¹ Cu, 2.47, 1.72, 2.96, and 3978.92 times that of the amount associated with the Cu-N-C-700, Cu-N-C-900, Cu-N-C-1000, and Cu plate-800 cathodes, respectively. These findings clearly support that the increasing size of Cu leads to reduction in the catalytic activity. The relatively worse performance of Cu-N-C-700 compared to Cu-N-C-800 for NO₃RR was likely due to the thick carbon layer hindering the Cu atoms from being fully accessed by the reactant.

Nitrite is a frequently detected intermediate during NO₃RR over Cu cathodes,^[17,26,37,38] but it is an undesirable by-product due to its greater toxicity than nitrate. An interesting note, as shown in Figure 3c, is that a very low level of NO₂⁻-N was detected in the Cu-N-C-700 and Cu-N-C-800 systems. The Cu-N-C-900 and Cu-N-C-1000 cathodes, however, yielded larger concentrations of NO₂⁻-N available in the solution. The reference Cu plate-800 system caused the most severe accumulation of nitrite. The selectivity of NO₂⁻-N for all the cathodes was

calculated based on the highest NO₂⁻-N concentration detected throughout the electrolysis process. Figure 3d further illustrates that the selectivity of NO₂⁻-N related to Cu-N-C-800 was only 5.0% (at 2 h), distinctly lower than 8.2% (at 2 h) of Cu-N-C-700, 16.1% (at 2 h) associated with Cu-N-C-900, 34.6% (at 2 h) relevant to Cu-N-C-1000, and 60.6% (at 6 h) corresponding to Cu plate-800. The NO₂⁻-N concentration began to decline with additional time after it reached the maximum because of its further reduction into other products. Less time was required for the complete disappearance of nitrite accumulation in the Cu-N-C-800 system. For Cu plate-800, 6.07 mg L⁻¹ of NO₂⁻-N remained even after 12 h of operation, which can be attributed to the fact that the bulk Cu surfaces show weak adsorption capacity for the nitrite intermediate generated from NO₃RR.^[27,39] Additional control experiments were conducted with electrocatalytic nitrite reduction on the Cu-N-C-T catalysts, and the results (Figure S6, Supporting Information) demonstrate that its reduction on Cu-N-C-800 occurs at a greater rate. The rate constant decreased in the order of Cu-N-C-800 (2.11×10^{-4} s⁻¹) > Cu-N-C-700 (1.85×10^{-4} s⁻¹) > Cu-N-C-900 (1.36×10^{-4} s⁻¹) > Cu-N-C-1000 (1.12×10^{-4} s⁻¹), implying that the metallic Cu nanoparticles are comparatively unfavorable for nitrite reduction. Notably, the rate constant of nitrite removal on the Cu-N-C cathodes was one order larger than that of nitrate reduction, confirming

that nitrite reduction is quicker and providing evidence that nitrate-to-nitrite conversion is a prerequisite for NO_3RR .^[12,40] The rate of $\text{NH}_4^+\text{-N}$ generation on the Cu-N-C-800 cathode was larger than that on the Cu-N-C-700, Cu-N-C-900, and Cu-N-C-1000 cathodes (Figure S6c, Supporting Information). Another interesting note is that the Cu-N-C-800 cathode elicited little accumulation of $\text{NO}_3^-\text{-N}$, as shown in Figure S6d (Supporting Information), while it existed in the Cu-N-C-900 and Cu-N-C-1000 systems owing to nitrite oxidation at the anode. It can be inferred from all of the above results that the single-atom active sites in Cu-N-C-800 are more beneficial to adsorption of free anions (such as NO_3^- and NO_2^-) and that their adsorption plays a crucial role in accelerating the reduction of nitrate and nitrite. Comparisons with reports in the literature concerning Cu-based electrocatalysts or porous carbon-supported metallic electrocatalysts of NO_3RR clearly indicate the uniqueness of single-atom Cu electrocatalysts with respect to the significant attenuation of nitrite release (Table S3, Supporting Information).

A significant generation of $\text{NH}_4^+\text{-N}$ was noticed for NO_3RR catalyzed by Cu-N-C-800. This appears to be much higher than that in other systems (Figure 3e), suggesting that nitrate is quickly converted into ammonia because of the reduced accumulation of nitrite during nitrate reduction. Notably, the slight reduction in the $\text{NH}_4^+\text{-N}$ concentration after 8 h of electrolysis in the Cu-N-800 system is due to the volatilization of ammonia as a result of the increased alkalinity caused by the consumption of protons by nitrate reduction and hydrogen evolution reaction,^[41] as elaborated in Text S1 and Figure S7 (Supporting Information). Figure 3f shows and compares the current efficiency that was calculated based on the data recorded from

the electrolysis test run over 12 h. It was apparent that the current efficiency of the Cu-N-C-800 cathode (19.5%) was greater than that of the Cu-N-C-700 (16.3%), Cu-N-C-900 (18.1%), and Cu-N-C-1000 (15.8%) cathodes but significantly lower than the value of Cu plate-800 (46.7%). The pronounced differentiation can be explained by the fact that metallic Cu is less sensitive to hydrogen evolution than the carbon nanosheet-structured carbon during electrolysis.^[42] Despite the relatively low current efficiency (19.5%) because of the competitive reaction of water electrolysis on the Cu-N-C-800 cathode, this value is larger than those reported for NO_3RR on carbon-supported metallic catalysts.^[8]

The influences of reaction time, cathodic potential, initial $\text{NO}_3^-\text{-N}$ concentration, and initial Cl^- concentration in the electrolyte on the electrocatalytic performance of Cu-N-C-800 for NO_3RR were evaluated in terms of the absolute amount of $\text{NO}_3^-\text{-N}$ removal, the current efficiency, and the selectivity for $\text{NO}_2^-\text{-N}$. As illustrated in Figure 4a, the prolonged electrolysis time resulted in an increase in the amount of $\text{NO}_3^-\text{-N}$ removal but a drop in the current efficiency. The decreased current efficiency from 58.6% (2 h) to 19.5% (12 h) was induced by the more intense competition for electrons by water with the prolongation of time. The $\text{NO}_2^-\text{-N}$ selectivity declined from 5.0% (2 h) to 0.2% (12 h), suggesting further conversion of nitrite into ammonia and/or nitrogen with increasing time.^[40,43,44] The cathodic potential is an important factor determining the extent of nitrate reduction as it represents a driving force propelling the reaction. The impact of cathodic potential on the proportions of $\text{NO}_3^-\text{-N}$, $\text{NO}_2^-\text{-N}$, and $\text{NH}_4^+\text{-N}$ as a function of time is illustrated in Figure S8 (Supporting Information). Figure 4b

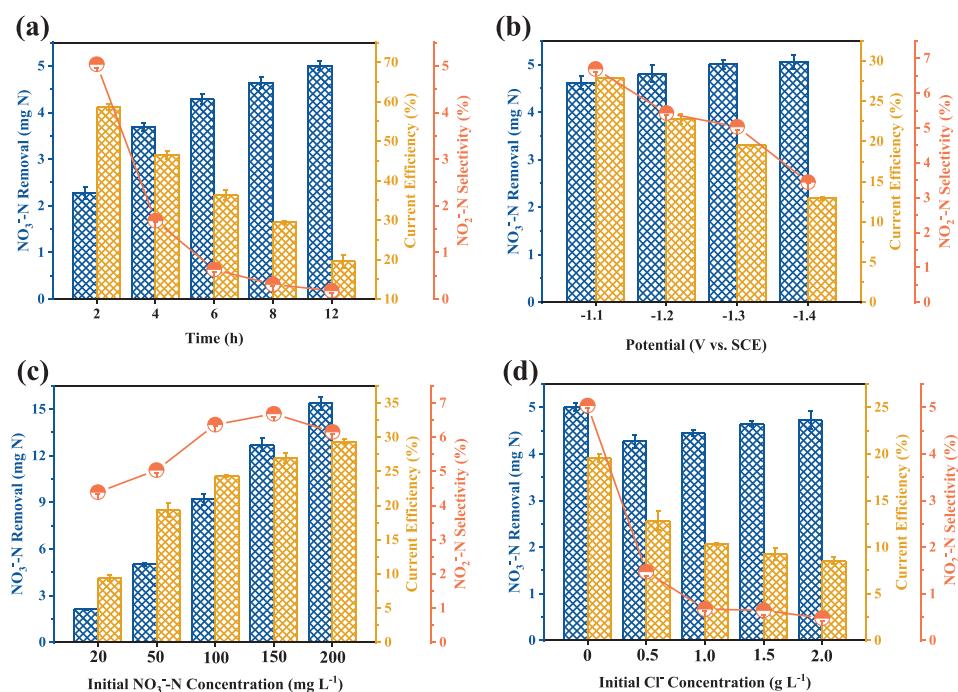
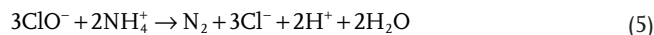
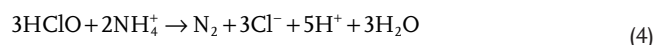
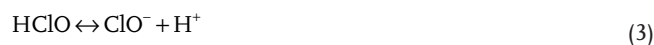


Figure 4. Effects of a) electrolysis time, b) cathodic potential, c) initial $\text{NO}_3^-\text{-N}$ concentration, and d) initial Cl^- concentration on $\text{NO}_3^-\text{-N}$ removal, current efficiency, and $\text{NO}_2^-\text{-N}$ selectivity for NO_3RR over Cu-N-C-800. For (b)–(d), the highest $\text{NO}_2^-\text{-N}$ selectivity was recorded throughout the electrolysis process. Reaction conditions: [initial $\text{NO}_3^-\text{-N}$] = 50 mg L^{-1} for (a), (b), and (d); [initial Cl^- concentration] = 0 for (a)–(c); cathodic potential = -1.3 V for (a), (c), and (d); electrolysis time = 12 h for (b)–(d); and $[\text{Na}_2\text{SO}_4]$ = 50×10^{-3} M.

illustrates that nitrate removal increased from 4.62 mg N at -1.1 V to 5.06 mg N at -1.4 V, when the Cu-N-C-800 cathode was run over 12 h. However, the more negative potentials caused a lower current efficiency (e.g., 19.5% at -1.3 V vs 12.9% at -1.4 V) because the excessive hydrogen evolution reaction was intensified when the cathodic potential shifted to more negative values.^[45,46] Nevertheless, the negative potential was beneficial in reducing NO_2^- -N selectivity (e.g., 5.0% at -1.3 V vs 3.4% at -1.4 V). For most of the tests, nitrate reduction was set at -1.3 V (the current density–time curve for the Cu-N-C-800 cathode is illustrated in Figure S9, Supporting Information) based on the consideration of nitrate removal rates higher than -1.1 and -1.2 V and current efficiency lower than -1.4 V.

Figure 4c shows the effect of the initial NO_3^- -N concentration on nitrate removal capacity. Although the percentage of NO_3^- -N removal gradually decreased (Figure S10a, Supporting Information), the absolute amounts of the removed NO_3^- -N after 12 h increased from 2.11 to 15.37 mg N as its initial concentration increased from 20 to 200 mg L^{-1} owing to the enhanced mass transfer at the high initial concentration. This can also explain the increased current efficiency with the increasing initial concentration of NO_3^- -N. The remaining percentage of NO_3^- -N was less than 15.3% when the Cu-N-C-800 system was fed with 200 mg L^{-1} NO_3^- -N and operated over 24 h (Figure S11, Supporting Information). This suggests that the Cu-N-C-800 cathode exhibits the capability of treating wastewater with high levels of nitrate. The increasing NO_3^- -N concentration did not yield an apparent increase in the selectivity of NO_2^- -N. Figure S10b (Supporting Information) shows that the maximum concentration of NO_2^- -N detected throughout the electrolysis was only 4.1 mg L^{-1} when the electrolyte contained 200 mg L^{-1} of NO_3^- -N, which was significantly lower than that of the pure Cu cathode.^[19,26,40] The result further confirms that the Cu-N-C-800 catalyst possesses an outstanding ability to reduce the accumulation of nitrite.

The presence of Cl^- in the electrolyte can favor the indirect electrochemical oxidation of ammonia to nitrogen, known as the breakpoint chlorination reaction between active chlorine (generated from anodic Cl^- oxidation) and ammonia (Equations (1)–(5)).^[47,48] Figure S12 (Supporting Information) depicts the effect of Cl^- concentration on the proportions of NO_3^- -N, NO_2^- -N, and NH_4^+ -N as a function of time. As evident in Figure S13 (Supporting Information), the NH_4^+ -N selectivity decreased remarkably from 96.3% in the absence of Cl^- to zero at 2.0 g L^{-1} of Cl^- after 12 h. Compared with the case without Cl^- , the presence of Cl^- led to a slight decline in the amount of NO_3^- -N removed (Figure 4d), which should be ascribed to the blockage of active sites by the adsorbed Cl^- . Nevertheless, the nitrate removal capacity gradually rose as a consequence of the increase in the Cl^- concentration. The NO_2^- -N selectivity decreased with the increasing Cl^- concentration. These results should be attributed to thermodynamically favorable nitrate reduction and nitrite reduction as a result of the remarkable decline in the concentration of NH_4^+ -N.



The long-term stability of Cu-N-C-800, a critical factor in the development of electrocatalysts, was investigated in repeatable electrolysis experiments under optimized conditions. As is apparent in Figure 5a, the electrocatalytic activity of the Cu-N-C-800 catalyst was well retained as the percentage of NO_3^- -N conversion was maintained in a narrow range from 100% to 92.8% as recorded over 20 consecutive cycles. In comparison with the first cycle, the percentage of NO_3^- -N conversion only declined by 5.4% with respect to the 20th cycle. Conversely, the Cu-N-C-900 and Cu-N-C-1000 catalyst suffered from a slight catalyst deactivation, indicated by a 7.9% and 10.1% drop in the tenth cycle compared with the first cycle (Figure S14, Supporting Information), respectively. A dramatic deterioration in the percentage of NO_3^- -N conversion from 34.9% (cycle 1) to 9.8% (cycle 5) was observed for the Cu plate-800 cathode. The dissolution, corrosion, and aggregation effects are considered to be responsible for the rapid catalyst decay.^[37,49] These results demonstrate that Cu atoms anchored on the carbon nanosheet offer superior electrocatalytic durability to metallic Cu. Figure 5b,c shows the TEM and the corresponding HAADF-STEM elemental mapping images of the cycled Cu-N-C-800. It can be seen that the nanosheet carbon structure with embedded Cu atoms was preserved, except that a small proportion of single atoms aggregated into nanoparticles. This explains the slight decrease in the catalytic activity in the latter cycles. Nevertheless, the XRD pattern in Figure 5d shows that, apart from the three peaks assigned to the nickel substrate, the Cu-N-C-800 cathode after 20 cycles of operation displayed no additional peaks as compared with the synthesized Cu-N-C-800 catalyst. The result strongly supports the determination that the majority of the Cu species appear in the form of single atoms. Moreover, the concentration of Cu^{2+} released to the electrolyte after tests were determined by inductively coupled plasma mass spectrometry (ICP-MS) and were found to be less than 774 $\mu\text{g L}^{-1}$, showing the negligible dissolution of Cu over long-term operation.

2.3. DFT Studies and Proposed Mechanism for NO_3RR on Cu-N-C-800

To understand the increased NO_3RR activity and the intriguing finding of the significant reduction in the release of nitrite attributed to the single Cu atoms, theoretical calculations on the adsorption energies of NO_3^- and NO_2^- on the catalyst surfaces were performed. It is well established that adsorption is the prerequisite step limiting overall rates of electrochemical nitrate and nitrite reduction.^[12,50] For comparison, the Cu-N₂ and Cu-N₄ moieties of the Cu–N bond predominant in Cu-N-C-800 and the Cu(111) facet of the Cu–Cu bond available in Cu-N-C-900 were selected as the active sites for adsorption of NO_3^- and NO_2^- (Figure S15, Supporting Information). As shown in Figure 6a, the calculated adsorption energy of NO_3^- on Cu(111) is 6.13 eV, which is much higher than that on Cu-N₂

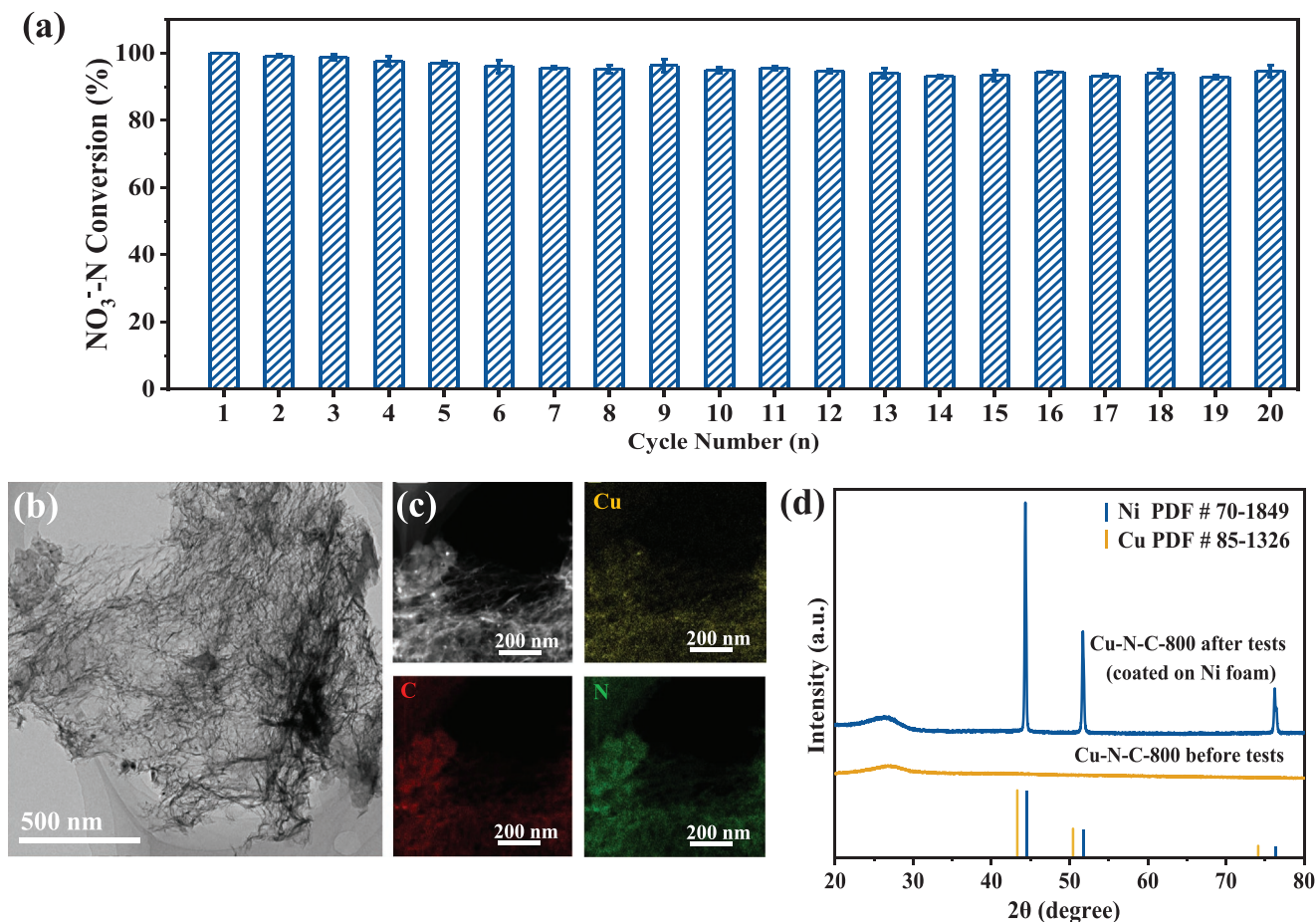
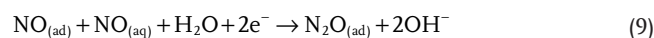
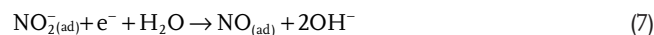
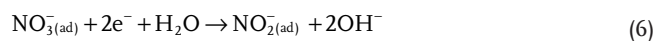


Figure 5. a) Durability tests of nitrate conversion; b) TEM image; and c) corresponding HAADF-STEM elemental mapping of Cu-N-C-800 after 20-cycle electrolysis tests. d) XRD patterns of the Cu-N-C-800 cathode before and after 20-cycle electrolysis tests. Reaction conditions: [initial NO₃⁻]= 50 mg L⁻¹; [Na₂SO₄]= 50 × 10⁻³ M; cathodic potential = -1.3 V; and electrolysis time = 24 h.

(-4.06 eV) and Cu-N₄ (-2.50 eV). This clearly indicates that the Cu-N_x active sites in the single Cu atoms are more favorable for NO₃⁻ adsorption than the Cu (111) plane in the Cu nanoparticles and explains the enhanced NO₃RR rates obtained with Cu-N-C-800 compared with Cu-N-C-900 and Cu plate-800.

According to the mechanistic pathway of NO₃RR reported in the literature,^[11,12] NO₃⁻ is firstly adsorbed on Cu sites and then reduced to NO₂⁻_(ad) (Equation (6)), and the selectivity of overall NO₃RR depends on the consecutive reduction of NO₂⁻_(ad). The adsorption of NO₂⁻ on the active sites is critical in initiating the reduction reaction of nitrate to ammonia and nitrogen; otherwise, nitrite is released into the solution in the free form. The calculations of adsorption energy starting with NO₂⁻ (Figure 6b) suggest that the Cu atoms (bound with N) with lower valence states have a stronger affinity to NO₂⁻, whereas Cu(111) surfaces exhibit a weaker capacity of adsorption of NO₂⁻. For the Cu-N-C-800 catalyst, there should be two primary pathways governing the formation of the end-products: ammonia via Equations (7) and (8) or nitrogen via Equations (7), (9), and (10).^[11] All these results demonstrate that NO₂⁻ is more prone to be adsorbed onto Cu-N_x (particularly Cu-N₂) and is easier to be desorbed from Cu(111), and

they provide solid evidence for low levels of nitrite accumulation in the Cu-N-C-800 system.



3. Conclusion

In conclusion, we have demonstrated that single Cu atoms stabilized by nitrogenated carbon nanosheet interact with NO₃⁻ and NO₂⁻ more strongly than the corresponding Cu nanoparticles and bulk metal. The calculation results show that Cu-N_x sites (particularly Cu-N₂) play a crucial role in favoring their

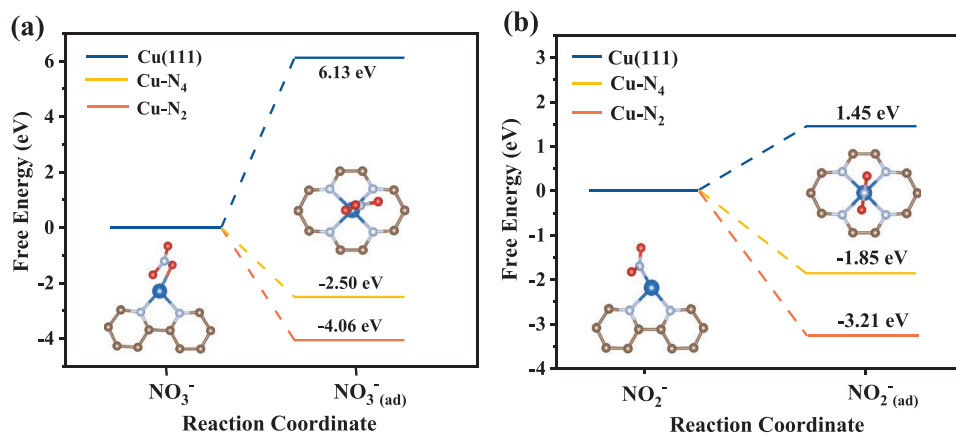


Figure 6. Calculated free energies for a) NO_3^- adsorption and b) NO_2^- adsorption on Cu (111), Cu-N₄, and Cu-N₂ surfaces, respectively. The brown, gray, blue, and red balls represent C, N, Cu, and O atoms, respectively.

adsorption. Consequently, single-atom Cu catalysts are effective in promoting NO_3RR at appreciably higher rates and, more importantly, in distinctly alleviating the release of nitrite to the solution. In addition, the single-atom Cu catalysts exhibit excellent stability after 20 consecutive cycles. These findings imply that downsizing Cu catalysts into single atoms is a promising route to improve their reactivity, selectivity, and stability in NO_3RR . This should open a new avenue for the design and construction of non-noble metal electrocatalysts for efficiently and selectively removing nitrate from aquatic ecosystems.

4. Experimental Section

Chemicals and Materials: Copper(II) acetate monohydrate ($\text{Cu}(\text{CO}_2\text{CH}_3)_2\text{H}_2\text{O}$, 99.95%), 1,3,5-benzenetricarboxylic acid (BTC, 98%), L-glutamic acid ($\text{C}_5\text{H}_9\text{NO}_4$, 99%), dicyandiamide (DCDA, $\text{C}_2\text{H}_4\text{N}_4$, 99.5%), and polytetrafluoroethylene preparation (PTFE, 60 wt%) were purchased from Sigma-Aldrich (USA). Potassium nitrate (KNO_3 , 99%), potassium nitrite (KNO_2 , 97%), hydrogen chloride (HCl, 37%), sodium sulfate anhydrous (Na_2SO_4 , 99%), sodium chloride (NaCl, 99.5%), and ethanol ($\text{CH}_3\text{CH}_2\text{OH}$, 99.5%) were obtained from Guangzhou Chemical Reagent Factory (China). Both Ni foam (used as the supporting substrate for electrocatalysts) and Cu plate ($3 \times 3.5 \times 0.2$ cm) (used as the control electrode for comparison) were purchased from Kunshan Guangjia Yuan New Materials Co., Ltd. (China).

Synthesis of the Single-Atom Cu Catalysts: The Cu-entrapped nitrogenated carbon nanosheets (labeled as Cu-N-C) were synthesized by the typical thermal method according to a previously reported process.^[51] For preparation of the precursor, BTC (1.160 g) was dissolved in deionized (DI) water (450 mL) and ethanol (50 mL), and then added into 500 mL of the solution containing $\text{Cu}(\text{CO}_2\text{CH}_3)_2\text{H}_2\text{O}$ (2.092 g) and L-glutamic acid (0.771 g). After stirring for 2 h at room temperature, the obtained precipitates were collected and washed with DI water and dried in vacuum at 40 °C overnight. Subsequently, the dried sample (0.10 g) was mixed with DCDA (1.00 g), and the mixture was ground into a homogeneous precursor in a mortar. It was then annealed at a selected temperature range of 700–1000 °C in an argon atmosphere with a ramping rate of 3 °C min^{-1} for 3 h. After cooling to room temperature, the product was successively leached with oxygen-saturated HCl (5 wt%) solution for 4 h to remove the freestanding metallic residues. The Cu-N-C catalysts were obtained and the synthesized samples were labeled as Cu-N-C-T, where T is the annealing temperature, an important factor to tailor the size of Cu in the nanosheet. For comparisons, BTC (0.10 g) and DCDA (1.00 g) were directly mixed by grinding and annealed

at 800 °C under the same conditions, with the resulting sample labeled as N-C-800; the Cu plate was also annealed at 800 °C (abbreviated as Cu plate-800).

Preparation of the Cu-N-C Cathode: The Ni foam (3.0 cm \times 3.5 cm) coated with the Cu-N-C catalysts served as the cathode. A homogeneous slurry was formed by mixing 80 mg of Cu-N-C, 12 mg of acetylene black, and 260 mg of PTFE (5 wt%). Then, this slurry was deposited on the Ni foam via a roller press and dried at 60 °C for 4 h and then at 120 °C for 12 h under vacuum.

Electrochemical Measurements: The nitrate reduction tests were carried out using a CHI 760E electrochemical workstation (Shanghai Chenhua Instrument Co., China) at -1.3 V in an undivided cell (100 mL) filled with 50 mg L^{-1} NO_3^- -N and 50×10^{-3} M Na_2SO_4 (as the supporting electrolyte). The Cu-N-C cathode, platinum foil (3 cm \times 3 cm), and saturated calomel electrode (SCE) were employed as the working electrode, counter electrode, and reference electrode, respectively. All the potentials were recorded against the SCE. Nitrite reduction tests were performed under similar conditions and were initiated with 20 mg L^{-1} NO_2^- -N. To examine the effects of different operating conditions on NO_3RR , additional experiments were performed under applied potentials ranging from -1.1 to -1.4 V, initial NO_3^- -N concentrations from 20 to 200 mg L^{-1} , and amended Cl^- concentrations from 0 to 2.0 g L^{-1} . 1 mL of solution was sampled at a predetermined time for the analysis of NO_3^- -N, NO_2^- -N, and NH_4^+ -N concentrations. All of the experiments were repeated at least three times. For comparison, the electrolysis experiments were also performed with the Cu plate-800 under the same conditions.

Physicochemical Characterizations: The surface morphology and crystalline structure of the Cu-N-C catalysts were examined using a field emission scanning electron microscope (SEM, Merlin, ZEISS Co., Germany), a STEM (Talos L120C, Thermo Fisher Scientific, USA), a double aberration-corrected scanning transmission electron microscope (Cs-corrected STEM, Themis G2 60-300, Thermo Fisher Scientific, USA), and XRD (Empyrean, Malvern Panalytical Co., UK). The surface elemental composition and the chemical states of different elements were characterized by XPS (ESCALAB250Xi, Thermo Fisher Scientific, USA). The XANES and EXAFS tests were conducted at beamline 44A in the Synchrotron Radiation Research Center in Taiwan. All the samples were characterized using Cu-K edge XANES and EXAFS in a transmission mode under ambient conditions. The concentration of Cu was measured by ICP-MS (iCAP RQ, Thermo Fisher Scientific, USA).

Density Functional Theory Calculations: The calculations of adsorption energies of NO_3^- and NO_2^- on the surfaces of various catalysts are detailed in Text S2 (Supporting Information).

Analytical Methods and Data Analysis: The concentrations of NO_3^- -N, NO_2^- -N, and NH_4^+ -N were determined with a UV-visible spectrophotometer (UV-vis, Evolution 300, Thermo Fisher Scientific,

USA). The concentration of N_2O was measured by analyzing the gaseous samples withdrawn from the headspace of the electrochemical cell using a gas chromatograph (7890A, Agilent Technologies Inc., USA). It should be noted that negligible amounts of gaseous N_2O were detected. Text S3 (Supporting Information) presents the equations applied to calculate the percentages of NO_3^- -N removal, NO_2^- -N generation, and NH_4^+ -N generation; the selectivity of NO_2^- -N and NH_4^+ -N; and the current efficiency of the nitrate reduction.

Supporting Information

Supporting Information is available from the Wiley Online Library or from the author.

Acknowledgements

The authors gratefully acknowledge financial support from the National Natural Science Foundation of China (Nos. 21876052 and 21577041); the Guangdong Special Support Plan for Innovation Teams (2019BT02L218); the Guangdong Special Support Plan for Young Top-notch Talents (2019TQ05L179); the Science and Technology Program of Guangzhou, China (No. 201904010293); and the Science and Technology Planning Project of Guangdong Province, China (No. 2019A050510009).

Conflict of Interest

The authors declare no conflict of interest.

Keywords

ammonia selectivity, electrocatalysis, nitrate reduction reaction, nitrite accumulation, single-atom copper

Received: July 27, 2020

Revised: September 24, 2020

Published online:

- [1] C. Q. Yu, X. Huang, H. Chen, H. C. J. Godfray, J. S. Wright, J. W. Hall, P. Gong, S. Q. Ni, S. C. Qiao, G. R. Huang, Y. C. Xiao, J. Zhang, Z. Feng, X. Ju, P. Ciaisi, N. C. Stenseth, D. O. Hessen, Z. L. Sun, L. Yu, W. J. Cai, H. H. Fu, X. M. Huang, C. Zhang, H. B. Liu, J. Taylor, *Nature* **2019**, 567, 516.
- [2] P. Clauwaert, K. Rabaey, P. Aelterman, L. De Schampelaire, T. H. Pham, P. Boeckx, N. Boon, W. Verstraete, *Environ. Sci. Technol.* **2007**, 41, 3354.
- [3] R. Epsztein, O. Nir, O. Lahav, M. Green, *Chem. Eng. J.* **2015**, 279, 372.
- [4] A. D. Fonseca, J. G. Crespo, J. S. Almeida, M. A. Reis, *Environ. Sci. Technol.* **2000**, 34, 1557.
- [5] F. D. Belkada, O. Kitous, N. Drouiche, S. Aoudj, O. Bouchelaghem, N. Abdi, H. Grib, N. Mameri, *Sep. Purif. Technol.* **2018**, 204, 108.
- [6] R. Mukherjee, S. De, *J. Membr. Sci.* **2014**, 466, 281.
- [7] W. Teng, N. Bai, Y. Liu, Y. P. Liu, J. W. Fan, W. X. Zhang, *Environ. Sci. Technol.* **2018**, 52, 230.
- [8] W. J. Duan, G. Li, Z. C. Lei, T. H. Zhu, Y. Z. Xue, C. H. Wei, C. H. Feng, *Water Res.* **2019**, 161, 126.
- [9] H. Xu, J. Wu, W. Luo, Q. Li, W. X. Zhang, J. P. Yang, *Small* **2020**, 16, 2001775.
- [10] C. Chen, K. Li, C. Li, T. H. Sun, J. P. Jia, *Environ. Sci. Technol.* **2019**, 53, 13868.
- [11] S. G. Segura, M. L. Lopes, K. Hristovski, P. Westerhoff, *Appl. Catal., B* **2018**, 236, 546.
- [12] V. Rosca, M. Duca, M. T. De Groot, M. T. M. Koper, *Chem. Rev.* **2009**, 109, 2209.
- [13] R. R. Jia, Y. T. Wang, C. H. Wang, Y. F. Ling, Y. F. Yu, B. Zhang, *ACS Catal.* **2020**, 10, 3533.
- [14] Y. H. Wang, A. N. Xu, Z. Y. Wang, L. S. Huang, J. Li, F. W. Li, J. Wicks, M. C. Luo, D. H. Nam, C. S. Tan, Y. Ding, J. W. Wu, Y. W. Lum, C. T. Dinh, D. Sinton, G. F. Zheng, E. H. Sargent, *J. Am. Chem. Soc.* **2020**, 142, 5702.
- [15] Y. T. Wang, W. Zhou, R. R. Jia, Y. F. Yu, B. Zhang, *Angew. Chem., Int. Ed.* **2020**, 59, 5350.
- [16] J. Li, G. M. Zhan, J. H. Yang, F. J. Quan, C. L. Mao, Y. Liu, B. Wang, F. C. Lei, L. J. Li, A. W. M. Chan, L. P. Xu, Y. B. Shi, Y. Du, W. C. Hao, P. K. Wong, J. F. Wang, S. X. Dou, L. Z. Zhang, J. C. Yu, *J. Am. Chem. Soc.* **2020**, 142, 7036.
- [17] C. Roy, J. Deschamps, M. H. Martin, E. Bertin, D. Reyter, S. Garbarino, L. Roué, D. Guay, *Appl. Catal., B* **2016**, 187, 399.
- [18] D. Çirimi, R. Aydın, F. Köleli, *J. Electroanal. Chem.* **2015**, 736, 101.
- [19] T. Y. Wu, X. G. Kong, S. Y. Tong, Y. Chen, J. Liu, Y. Tang, X. J. Yang, Y. M. Chen, P. Y. Wan, *Appl. Surf. Sci.* **2019**, 489, 321.
- [20] Z. Li, S. F. Ji, Y. W. Liu, X. Cao, S. B. Tian, Y. J. Chen, Z. Q. Niu, Y. D. Li, *Chem. Rev.* **2020**, 120, 623.
- [21] T. Zhang, D. Zhang, X. H. Han, T. Dong, X. W. Guo, C. S. Song, R. Si, W. Liu, Y. F. Liu, Z. K. Zhao, *J. Am. Chem. Soc.* **2018**, 140, 16936.
- [22] M. H. Li, H. F. Wang, W. Luo, P. C. Sherrell, J. Chen, J. P. Yang, *Adv. Mater.* **2020**, 32, 2001848.
- [23] X. Y. Li, H. P. Rong, J. T. Zhang, D. S. Wang, Y. D. Li, *Nano Res.* **2020**, 13, 1842.
- [24] Y. X. Guan, Y. Y. Feng, J. Wan, X. H. Yang, L. Fang, X. Gu, R. R. Liu, Z. Y. Huang, J. Li, J. Luo, C. M. Li, Y. Wang, *Small* **2018**, 14, 1800697.
- [25] Z. Mácová, K. Bouzek, J. Šerák, *J. Appl. Electrochem.* **2007**, 37, 557.
- [26] X. D. Wang, M. Q. Zhu, G. S. Zeng, X. Liu, C. Fang, C. H. Li, *Nanoscale* **2020**, 12, 9385.
- [27] L. Durivault, O. Brylev, D. Reyter, M. Sarrazin, D. Bélanger, L. Roué, *J. Alloys Compd.* **2007**, 432, 323.
- [28] S. H. Ma, Z. Han, K. Y. Leng, X. J. Liu, Y. Wang, Y. T. Qu, J. B. Bai, *Small* **2020**, 16, 2001384.
- [29] P. Yang, S. W. Zuo, F. T. Zhang, B. Yu, S. E. Guo, X. X. Yu, Y. F. Zhao, J. Zhang, Z. M. Liu, *Ind. Eng. Chem. Res.* **2020**, 59, 7327.
- [30] Y. F. Li, M. H. Kong, J. P. Hu, J. S. Zhou, *Adv. Energy Mater.* **2020**, 10, 2000400.
- [31] Y. T. Qu, Z. J. Li, W. X. Chen, Y. Lin, T. W. Yuan, Z. K. Yang, C. M. Zhao, J. Wang, C. Zhao, X. Wang, F. Y. Zhou, Z. B. Zhuang, Y. Wu, Y. D. Li, *Nat. Catal.* **2018**, 1, 781.
- [32] W. T. Wei, Y. Z. Lu, W. Chen, S. W. Chen, *J. Am. Chem. Soc.* **2011**, 133, 2060.
- [33] G. K. Han, Y. Zheng, X. Zhang, Z. Q. Wang, Y. Gong, C. Y. Du, M. N. Banis, Y. M. Yiu, T. K. Sham, L. Gu, Y. R. Sun, Y. J. Wang, J. P. Wang, Y. Z. Gao, G. P. Yin, X. L. Sun, *Nano Energy* **2019**, 66, 104088.
- [34] C. Z. Zhu, S. F. Fu, J. H. Song, Q. R. Shi, D. Su, M. H. Engelhard, X. L. Li, D. D. Xiao, D. S. Li, L. Estevez, D. Du, Y. H. Lin, *Small* **2017**, 13, 1603407.
- [35] H. H. Wu, H. B. Li, X. F. Zhao, Q. F. Liu, J. Wang, J. P. Xiao, S. H. Xie, R. Si, F. Yang, S. Miao, X. G. Guo, G. X. Wang, X. H. Bao, *Energy Environ. Sci.* **2016**, 9, 3736.
- [36] D. H. Wang, C. C. Ao, X. K. Liu, S. Fang, Y. Lin, W. Liu, W. Zhang, X. S. Zheng, L. D. Zhang, T. Yao, *ACS Appl. Energy Mater.* **2019**, 2, 6497.

- [37] S.-E. Bae, K. L. Stewart, A. A. Gewirth, *J. Am. Chem. Soc.* **2007**, *129*, 10171.
- [38] D. Reyter, D. Bélanger, L. Roué, *Electrochim. Acta* **2008**, *53*, 5977.
- [39] O. S. G. P. Soares, J. J. M. Órfão, M. F. R. Pereira, *Catal. Lett.* **2008**, *126*, 253.
- [40] Y. J. Shih, Z. L. Wu, C. Y. Lin, Y. H. Huang, C. P. Huang, *Appl. Catal., B* **2020**, *273*, 119053.
- [41] C. Li, K. Li, C. Chen, Q. L. Tang, T. H. Sun, J. P. Jia, *Sep. Purif. Technol.* **2020**, *237*, 116485.
- [42] C. Wei, Y. M. Sun, G. G. Scherer, A. C. Fisher, M. Sherburne, J. W. Ager, Z. J. Xu, *J. Am. Chem. Soc.* **2020**, *142*, 7765.
- [43] W. Teng, J. W. Fan, W. X. Zhang, *ACS Appl. Mater. Interfaces* **2020**, *12*, 28091.
- [44] C. A. Clark, C. P. Reddy, H. Xu, K. N. Heck, G. H. Luo, T. P. Senftle, M. S. Wong, *ACS Catal.* **2020**, *10*, 494.
- [45] E. P. Gallent, M. C. Figueiredo, I. Katsounaros, M. T. M. Koper, *Electrochim. Acta* **2017**, *227*, 77.
- [46] J. P. Shi, D. L. Ma, G. F. Han, Y. Zhang, Q. Q. Ji, T. Gao, J. Y. Sun, X. J. Song, C. Li, Y. S. Zhang, X. Y. Lang, Y. F. Zhang, Z. F. Liu, *ACS Nano* **2014**, *8*, 10196.
- [47] L. Su, D. D. Han, G. J. Zhu, H. Xu, W. Luo, L. J. Wang, W. Jiang, A. G. Dong, J. P. Yang, *Nano Lett.* **2019**, *19*, 5423.
- [48] Y. Lan, J. L. Chen, H. Zhang, W. X. Zhang, J. P. Yang, *J. Mater. Chem. A* **2020**, *8*, 15853.
- [49] G. E. Dima, A. C. A. De Vooy, M. T. M. Koper, *J. Electroanal. Chem.* **2003**, *554*, 15.
- [50] C. C. Sun, F. W. Li, H. An, Z. K. Li, A. M. Bond, J. Zhang, *Electrochim. Acta* **2018**, *269*, 733.
- [51] F. Li, G. F. Han, H. J. Noh, S. J. Kim, Y. L. Lu, H. Y. Jeong, Z. P. Fu, J. B. Baek, *Energy Environ. Sci.* **2018**, *11*, 2263.